Small and ultra small angle neutron scattering on pure and supramolecular composite GelMA hydrogels

Harrison Porritt, Anaïs Chalard, Juliette Fitremann, Jitendra Mata, Jenny Malmström

Journal of Colloid and Interface Science 700 (2025) 138443

Contents lists available at ScienceDirect

Journal of Colloid And Interface Science

journal homepage: www.elsevier.com/locate/jcis

Small and ultra small angle neutron scattering on pure and supramolecular composite GelMA hydrogels

Harrison Porritt [a,b], Anaïs Chalard [a,b], Juliette Fitremann [c], Jitendra Mata [d,e,**], Jenny Malmström [a,b,*]

[a] Department of Chemical and Materials Engineering, Faculty of Engineering and Design, The University of Auckland, Auckland, New Zealand
[b] The MacDiarmid Institute for Advanced Materials and Nanotechnology, Wellington, New Zealand
[c] Laboratoire Softmat, Université de Toulouse, CNRS UMR, 5623 Toulouse, France
[d] Australian Centre for Neutron Scattering, Australian Nuclear Science and Technology Organization, Lucas Heights, NSW 2234, Australia
[e] School of Chemistry, University of New South Wales, Sydney 2052, Australia

HIGHLIGHTS

- Extensive network characterization of GelMA hydrogels across varying crosslinking densities and corresponding Young's moduli.
- Identification of densely crosslinked aggregates uniquely present in stiff GelMA hydrogels.
- GalC7 supramolecular fibre incorporation causes minimal disruption to the GelMA hydrogel network.

GRAPHICAL ABSTRACT

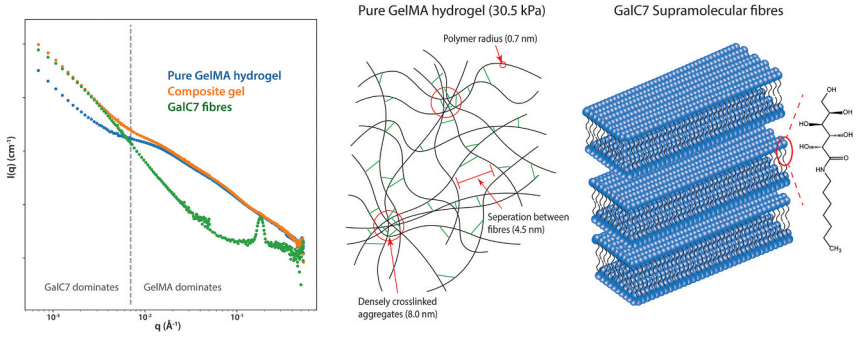

ARTICLE INFO

Keywords:
Gelatin methacryol
Stiffness change
SANS/USANS
Supramolecular hydrogels
Galactonamides

ABSTRACT

Development of highly sophisticated tissue-engineered models capable of eliciting specific health and disease states could revolutionise disease treatment. To accomplish this it requires the generation of highly sophisticated hydrogel/biomaterial systems, including materials with tuneable properties and multiscale architecture composed of structures with different sizes ranges. In developing such systems, it is crucial to quantify any structures and interactions in the nano- and micron-scale range, to determine how these systems may affect cell phenotype. Small and ultra-small angle neutron scattering were used to quantify the structure of two biomaterials previously used in tissue engineering techniques. Gelatin methacryloyl (GelMA) is a commonly used hydrogel for tissue engineering and it has already been established that its Young's modulus can be tuned by controlling the crosslinking density. In this work, neutron scattering showed that there is little difference between the mesh size/fibre spacing (4.7 nm–4.5 nm) in 9.1 % w/v, soft (7.3 kPa ± 2.2 kPa), low crosslinked GelMA hydrogels and stiff (30.5 kPa ± 3.5 kPa), highly crosslinked GelMA hydrogels. However, stiff GelMA

* Corresponding author at: Department of Chemical and Materials Engineering, Faculty of Engineering and Design, The University of Auckland, Auckland, New Zealand.
** Corresponding author at: Australian Centre for Neutron Scattering, Australian Nuclear Science and Technology Organization, Lucas Heights, NSW 2234, Australia.
E-mail addresses: jtm@ansto.gov.au (J. Mata), j.malmstrom@auckland.ac.nz (J. Malmström).

https://doi.org/10.1016/j.jcis.2025.138443
Received 7 May 2025; Received in revised form 2 July 2025; Accepted 13 July 2025
Available online 18 July 2025

hydrogels showed the formation of dense highly crosslinked aggregates with a size of 8.0 nm that were not seen in the soft GelMA hydrogels. Neutron scattering was also performed on newly developed composite hydrogels consisting of GelMA (polymer chain radius 0.7 nm) embedded with significantly larger supramolecular fibres made from stacked bilayers of N-heptyl-galactonamides. Previously characterised pure galactonamide fibres were confirmed to have a thickness of 128 nm with a repeatable stacking/bilayer thickness of 3.7 nm. Incorporation of such large galactonamide fibres within the GelMA led to no disruption of the GelMA network.

1. Introduction

Recent advancements in tissue engineering have centred on developing more sophisticated hydrogel-based systems that better represent the extracellular matrix (ECM) of native tissue. Hydrogels are a class of materials used in tissue engineering that mimic some of the vital properties of ECM, such as being highly hydrated and sometimes made of fibrous materials, which are ideal for cell attachment, growth and migration in 3D [1–3]. Hydrogels can be made from natural materials such as alginate [4], collagen [5] or hyaluronic acid [6] or synthetic polymers such as polyethylene glycol [7] or polyacrylamide [8]. The development of multi-scale composite hydrogels, with finely tuned mechanical properties, could facilitate breakthroughs in regenerative medicine and improve our understanding of tissue function in both healthy and diseased states [9–11]. Composite gels that provide control over local mechanical properties and gel porosity, separately from macroscopic mechanical properties are particularly relevant to guide and control cell fate within tissue engineering models. The detailed structure of such composite hydrogels spans a wide range of size scales, from that of individual polymer chains and the size of pores, to that of larger incorporated fibres. To understand cell responses to such systems, we must first understand the structure of such complex gels.

Small and ultra small-angle neutron scattering (SANS and USANS or (U)SANS) are powerful techniques used to study the structure of materials across the relevant length scales for such composite gels, typically between 1 nm to 20 μm. During (U)SANS, a beam of neutrons is directed at a sample. Neutrons interact with the nuclei of the atoms in the material, causing them to scatter at a small angle. The angle at which the neutrons scatter at can provide information about the structures on the nano- and micron-scale [12,13]. In hydrogels, (U)SANS can characterise the morphology of specific structures, such as polymer radius and pore size/ porosity, as well as the density of connections (i.e. interactions) between polymers [14], all of which are known to affect the phenotype of cells cultured in such hydrogels [15–17]. Other commonly used characterization techniques, such as scanning electron microscopy (SEM) [18,19] and cryogenic scanning electron microscopy (Cryo-SEM) [20,21], can provide detailed visualisation of the sample surface at the nanometre scale. However, such methods require stringent sample preparation, such as freeze drying (SEM), or freezing (cryo-SEM), which can alter or damage the hydrogel's microarchitecture. The impact of freezing or drying is often underestimated, leading to an overestimation of the hydrogel's pore size [22].

One rising focus has emerged on using modified gelatin polymers as a hydrogel for tissue engineering [23–27]. Gelatin itself forms physical crosslinks upon cooling, but these crosslinks are not strong enough to form stable gels at physiological temperatures. To rectify this, modified versions of gelatin that allow for covalent crosslinking are often used. One such modified version is gelatin methacryloyl (GelMA), an engineered gelatin-based biomaterial obtained by the methacrylation of the amino groups, primarily the lysine residues, in the gelatin backbone using methacrylic anhydride. The methacrylic groups can form covalent bonds through free radical polymerization, forming crosslinks between adjacent gelatin strands resulting in a hydrogel that is stable at physiological temperatures [28]. GelMA hydrogels are most commonly photo-crosslinked using photoiniators sensitive to ultraviolet (UV) or visible light, these can include Irgacure 2595 [29], lithium acylphosphinate (LAP) [30] and eosin Y [23]. Photoinitiators sensitive to visible light have been preferred over ones sensitive to UV light as UV light can be cytotoxic to cells [31]. One emerging visible light–initiating system that has gained traction recently consists of a ruthenium (Ru)-based transition metal complex and sodium persulfate (SPS) [27,32]. When irradiated with blue light (450 nm wavelength), photolysis of Ru^{2+} into Ru^{3+} (high oxidation state) occurs, donating electrons to SPS. SPS dissociates into sulfate anions and sulfate radicals, which allows methacryloyl groups to form covalent bonds [32].

GelMA and other crosslinkable hydrogels are particularly useful in modelling diseases associated with changes in tissue stiffness, as the density of formed crosslinks can be used to finely tune the Young's modulus of the hydrogel. Hydrogels with controlled mechanical properties allow researchers to model diseases, such as cardiac scar formation [44], Alzheimer's [33], and osteoarthritis [34], all of which are associated with changes in tissue stiffness. Several studies demonstrated this ability to finely tune the mechanical properties of GelMA hydrogels by modulating the light intensity/duration during crosslinking [23,25,32,35–40], which, by extension, modulates the crosslink density. For example, we have previously demonstrated that the Youngs modulus of 10 % w/v GelMA hydrogels could be tuned from 10 kPa to 50 kPa by changing the irradiation time during crosslinking for the purpose of mimicking the environment of healthy and fibrotic cardiac tissue [23]. Studies have also shown that changes in cell mechanotransduction can directly result in changes in cell phenotype, such as chondrogenesis [16,41–43], and the fibroblast to myofibroblast transition [44–46]. However, increased hydrogel stiffness is usually associated with a decrease in porosity/pore size in crosslinkable hydrogels. While the effects of porosity and stiffness are challenging to decouple,it has been demonstrated that a decrease in porosity resulted in similar changes in cell phenotype to that of increased stiffness [16]. It is therefore important to have detailed studies of commonly used hydrogel systems like GelMA that characterises the nano- and micro-structure, as well as the mechanical properties.

Hydrogels made of a single material are generally not able to fully replicate the complex structure and hierarchical nature of ECM, which consists of many different structures/proteins. Collagen is a key protein that aids in cell attachment, alignment and tissue development. Although gelatin is derived from the hydrolysis of collagen, gelatin is a denatured and unstructured protein product and doesn't recapitulate the size and structure of collagen fibres. Composite materials used for tissue engineering usually incorporate larger fibrillar structures within a smaller mesh to compensate for this discrepancy. Artificial fibres such as electrospun poly(ε-caprolactone) (PCL) fibres [47,48] or carbon nanotubes [49], which can be incorporated into hydrogel scaffolds with good control over their structure and anisotropy, can be used. However, producing artificial polymer fibres can include the use of toxic solvents and may additionally need to be functionalised with cell adhesion sites to allow for cell attachment. Composite materials can also be created using different biocompatible fibrous proteins such as collagen or fibrin [29,30,32] that naturally have cell adhesion sites; however, achieving good control over the fibre's structure and size is much more complicated.

Supramolecular self-assembling molecules/low-molecular-weight gelators (LMWG) have recently been used in tissue engineering applications to make self-assembling structures which are assembled via non-covalent interaction between LMWGs [24,50,51]. Self-assembly usually results in the formation of fibres or ribbon-like structures [52], which

are referred to as supramolecular fibres, that are quite favourable to cell migration [50]. The shape and dimensions of the supramolecular fibre can be tuned by using either different LMWGs [53,54], or by changing the gelation conditions (temperature, pH, solvent shift) [52]. Supramolecular fibres have garnered more attention as of late, by being integrated into composite hydrogel scaffolds to mimic larger naturally occurring fibres [24,55]. A new supramolecular fibre used the LMWG, N-heptyl-galactonamide (GalC7), to form a fibrous network that supported neural cell culture [50]. This has subsequently been incorporated into GelMA hydrogels [24] by dissolving the LMWG at high temperatures, then upon cooling the molecules self-assembled to form long ribbon-like structures within the gel. This was confirmed to be biocompatible with cardiac fibroblasts [24].

This paper analyses two different hydrogel-based systems using SANS and USANS to understand the microarchitecture and the impact it may have on cell biology. Pure GelMA hydrogels at relatively low Young's modulus (<10 kPa) and relatively high Young's modulus (>30 kPa) are investigated to see how changes in stiffness affect the structure, arrangement and porosity of the hydrogel, at the nano and micron length scales. Composite hydrogels are additionally characterised, which combine GelMA with GalC7 derived supramolecular fibres. An illustration of the composite GelMA GalC7 system is provided in Fig. 1.

2. Experimental section

2.1. Materials

Solutions were prepared using ultrapure water (Type 1) from a Milli-Q Direct 8 water purification system, which has a resistivity of 18.2 MΩ·cm. Gelatin, methacrylic anhydride, Ruthenium photoiniator tris (2,2-bipyridyl)dichlororuthenium(II) hexahydrate (Ru), sodium persulfate (SPS), (3-aminopropyl) triethoxysilane, dichlorodimethylsilane, D_2O (for (U)SANS measurements) and cellulose dialysis tubing were obtained from Sigma-Aldrich (Auckland, New Zealand). Gibco phosphate-buffered saline (PBS) tablets were purchased from Life Technologies (Auckland, New Zealand). N-heptyl-galactonamide (GalC7) was provided by softmat lab (Toulouse, France).

2.2. GelMA synthesis

GelMA was synthesized following Loessners et al.'s protocol [26]. Gelatin (porcine skin, Type A, gel strength 300) was dissolved at 10 % wt/v in PBS for 1 h at 50 °C with constant stirring. Methacrylic anhydride (0.6 g per gram of gelatin) was added dropwise (10 mL/h) and allowed to react under continuous stirring for 3 h at 50 °C. The mixture was then centrifuged at 2000 RPM to remove unreacted methacrylic anhydride, diluted 2× with PBS, and dialyzed (MWCO 12,400 kDa) against Milli-Q Type 1 water for 7 days at 40 °C. The purified GelMA was frozen at −20 °C, freeze-dried for 5 days, and stored at −20 °C until use, with regular freeze-drying to prevent water accumulation. This produced lyophilised GelMA with a degree of functionalisation of ~80 % and was verified using a ninhydrin assay [23].

2.3. Determination of the degree of functionalization of GelMA

Following the protocol of Zatorski et al. [56], a ninhydrin assay was conducted to assess the synthesized GelMA's degree of functionalization. A 10 mg/mL gelatin solution was prepared and serially diluted to concentrations of 90 %, 80 %, 70 %, 60 %, 50 %, 40 %, 30 %, 20 %, and 10 % in PBS. Separately, a GelMA solution in PBS was prepared at a nominal concentration (C_{nom}) of 10 g/L. A ninhydrin solution (20 g/L) was also prepared in ethanol. The gelatin and GelMA solutions were

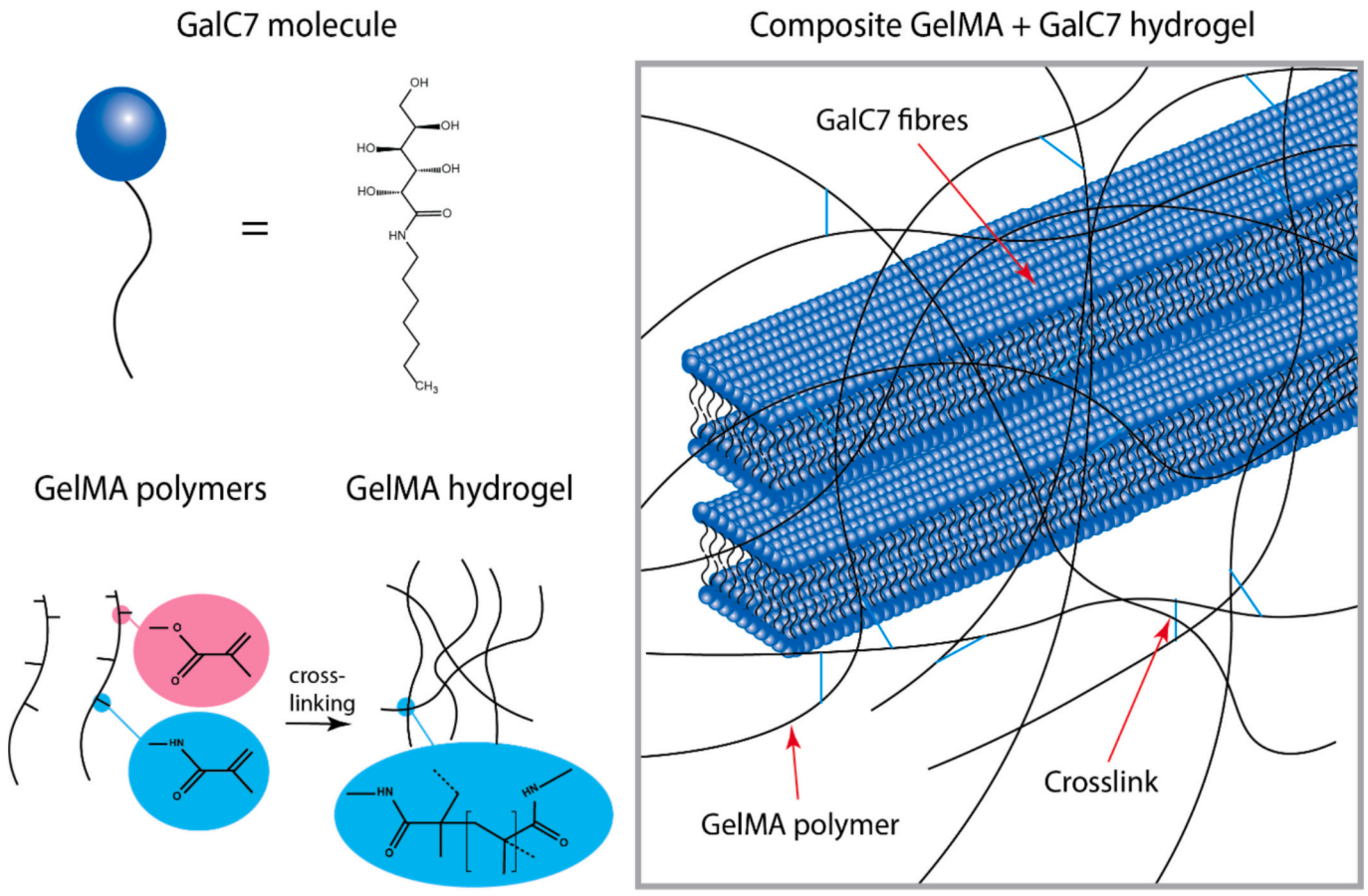

Fig. 1. Illustration of the composite hydrogel system derived from Galc7 supramolecular fibres and GelMA.

then mixed with the ninhydrin solution at a 1:8 volume ratio (corresponding to a final ninhydrin concentration of 2.2 g/L) and heated at 70 °C for 12 min without stirring. Triplicate samples of each solution were transferred to a 96-well plate, and their absorbance at 570 nm was measured at room temperature (RT). A calibration curve was constructed by plotting the absorbance of gelatin solutions against their respective concentrations, applying a linear fit to the range of 2–8 g/L. The "apparent concentration" (C_{app}) of GelMA, expressed in g/L, was determined by mapping the average absorbance of the GelMA solutions onto this linear fit. The fraction of available amine groups (f) in GelMA was then calculated as:

$$f = \frac{C_{app}}{C_{nom}} \tag{1}$$

Finally, the degree of functionalization (DoF) was computed using the formula:

$$\text{DoF}\ (\%) = 100 \times (1 - f) \tag{2}$$

2.4. Preparation of hydrophobic glass surfaces

Glass was cleaned by sonication in acetone for 15 min and exposed to UV ozone for 20 min. Dichlorodimethylsilane was applied to each side of the glass and left to react for approximately 2 min. Excess silane was wiped off with paper, and the functionalized glass was rinsed with Milli-Q Type 1 water.

2.5. Preparation of pure GelMA hydrogels

Freeze-dried GelMA was dissolved in PBS at a concentration of 11 % wt/v at 37 °C and vortexed intermittently until homogenized. Photoinitiators were prepared the day before by dissolving Ru and SPS in milli-Q water separately at concentrations of 8 mM and 40 mM, respectively, and kept wrapped in tinfoil at room temperature. The pre-gel solution was prepared by mixing 1.9 mL of 11 % wt/v GelMA solution with 100 µL of Ru solution and 100 µL of SPS solution. The final concentrations of GelMA, Ru, and SPS were 9.1 % wt/v, 0.38 mM, and 1.9 mM, respectively. 1.6 mL of the pre-gel solution was pipetted into a circular mould on a hydrophobic glass petri dish; the mould had a thickness of 1 mm each and a radius of 30 mm. This was covered with a hydrophobic coverslip and crosslinked at room temperature (RT) under a white-light LED lamp (76.9 W/m^2) over the wavelength range of 400–650 nm, (Mitre 10, New Zealand) for the appropriate time: 4 min (stiff) and 1 min (soft). For SANS and USANS measurements Samples were dried for shipping at room temperature over 3 days in a dark environment, then rehydrated in D_2O PBS with 0.025 % NaN_3 for 24 h before scattering, to increase contrast between the GelMA and solvent (see Table 1 for neutron scattering length densities). Samples were cut to size for SANS experiments with a radius of 20 mm to load into SANS demountable cells.

2.6. Preparation of pure GalC7 fibres

Pure GalC7 samples were prepared at the Australian Nuclear Science and Technology Organization (ANSTO) in Lucas Heights because they tend to undergo synaeresis (water-gel demixing) if they are shaken during transportation. N-heptyl-galactosamine was added to D_2O PBS at a concentration of 0.45 % wt/v in a sealed glass vial and heated at 105 °C in a block heater until complete dissolution of the powder (<10 min). The solution was pipetted directly into the SANS demountable holder and cooled at room temperature or in an oven at 100 °C, which was then set to 37 °C and cooled over roughly 30 min. The scattering length densities (SLD) of D_2O, H_2O, GelMA and GalC7 are listed in Table 1 and were calculated using the online SLD calculator (https://www.ncnr.nist.gov-/resources/activation/).

Table 1
Neutron scattering length densities.

Name	Scattering length density ($\times 10^{-6}$ Å^{-2})
D_2O	6.35
H_2O	−0.55
GelMA	3.25
GalC7	0.524

2.7. Preparation of composite hydrogels

A 0.45 % wt/v GalC7 solution was prepared in PBS as described above. Once the GalC7 powder was fully dissolved, the appropriate amount of freeze-dried GelMA was added to the GalC7 solution to make an 11 % wt/v solution of GelMA in the GalC7 solution and left at 105 °C in the block heater for 3 min to ensure complete dissolution of the GelMA. The glass vial was then transferred to an oven set at 100 °C for 5 min before the temperature was set to 37 °C to allow gradual cooling. Upon reaching 37 °C (approximately 3 h), 1.9 mL of the GalC7-GelMA solution was carefully pipetted (using a cut pipette tip to enlarge the opening) and mixed with 100 µL of 8 mM Ru solution in milli-Q water and 100 µL of SPS solution in milli-Q water. The solution was homogenized by gentle aspiration using a cut pipette tip. 1.6 mL of the pre-gel solution was pipetted into circular moulds, 1 mm thickness x 30 mm diameter for USANS samples, and 800 µL into moulds, 2 mm thickness x 20 mm diameter for SANS samples, moulds were placed on a hydrophobic glass petri dish. This was covered with a hydrophobic coverslip and crosslinked at room temperature (RT) under a white-light LED lamp (76.9 W/m^2, 400–650 nm) for 4 min. Samples were dried for shipping at room temperature over 3 days in a dark environment. Samples were rehydrated with D_2O PBS, to increase contrast between scattering of the hydrogels and the solvent (with 0.025 % NaN_3) for 1 h before scattering. Samples were rehydrated for only 1 h to prevent any dissolution of the GalC7 fibres within the gel [24].

2.8. Swelling ratio

To calculate the swelling ratio of pure GelMA hydrogels, gels were made measuring 40 mm diameter by 1 mm thickness (1.6 mL) at 4-min (stiff) and 1-min (soft) crosslinking durations. Gels were dried at room temperature for 3 days in a dark environment and then weighed. Gels were then submerged in 5 mL of PBS with 0.025 % NaN_3 and left for 24 h. Any surface water was wiped off prior to weighing. The apparent GelMA concentration was calculated using the formula (3):

$$\text{Swelling ratio} = \frac{m_{wet} - m_{dry}}{m_{dry}} \tag{3}$$

2.9. Force indentation with atomic force microscopy

Measurements were performed using an MFP-3D Origin AFM (Asylum Research, Santa Barbara, USA) in a liquid environment at room temperature to calculate the stiffness of the stiff and soft pure GelMA hydrogels. Pre-calibrated silicon nitride cantilevers with spring constants ranging from 0.07 to 0.08 N/m and a 5 µm glass bead at the tip (Novascan, USA) were used. To calibrate the DefInvols of the tip, force-indentation curves were recorded on a clean glass slide. Force maps were generated by performing 100 force indentations on the surface over an area of 90 µm × 90 µm and a tip velocity of 2 µm/s, and a trigger force of 5.0 nN. Force maps were analyzed using Asylum Research Software AR16 (version 16.10.211) in Igor Pro (version 6.38, WaveMetrics, USA), and the approach curve was fitted with the Hertz model [57]. The applied force (F_{app}) was fitted using the equation (4):

$$F_{app} = \frac{4}{3}\frac{E_s}{1-\theta_s^2}\sqrt{Rd^3} \tag{4}$$

where F_{app} is the applied force (N), E_s the Young's modulus (Pa), θ_s the

sample's Poisson ratio (0.33) [58], R the bead radius (m), and d the indentation depth (m). Histograms of Young's modulus were generated for each force map, with a Gaussian fit providing the mean modulus and standard deviation.

2.10. Small angle neutron scattering

SANS experiments were conducted using the Quokka SANS instrument at ANSTO [59]. Sample to detector distances of 2 m, 12 m, and 20 m (with lens optic) with neutron wavelengths of 5 Å (for 2 and 12 m detector distance) and 8.1 Å (for 20 m lens optic) were used to measure I (q) over a q-range of 0.0007 $Å^{-1}$ to 0.53 $Å^{-1}$. A 12.5 mm sample aperture was used for all configurations. Scattering was measured at constant temperatures of 37 °C. Samples were loaded into the Demountable Quokka cells (20 mm diameter, either 1 mm or 2 mm path length), and cells were topped up with degassed D_2O PBS. SANS data were reduced using NCNR macros (modified for Quokka) in Igor software, corrected for empty cell scattering, instrument background and transmission, and transformed to absolute scale using attenuated direct beam transmission [60]. Buffer background were subtracted using PRIMUS [61].

2.11. Ultra-small angle neutron scattering

USANS experiments were performed using the Kookaburra instrument at ANSTO with a neutron wavelength of 4.74 Å [62]. Swollen hydrogel was loaded into demountable Kookaburra cells (39 mm diameter and 1 mm path length) topped up with degassed D_2O PBS. Measurements were conducted at 37 °C with a 29 mm sample aperture, covering a q-range of 3.5×10^{-5} $Å^{-1}$ to 2.1×10^{-3} $Å^{-1}$. Data were reduced using Python scripts in Gumtree based on standard procedures [41] and de-smeared with the Lake algorithm via NIST USANS macros before merging with SANS data [60]. Structural parameters were determined by fitting the data to models using SasView (http://www.sasview.org/). Models were fitted by minimising the normalised error $(y_{pred}\text{-}y)/y$.

2.12. Attenuated total reflection Fourier transform infrared (ATR-FTIR) spectroscopy

Attenuated Total Reflection Fourier Transform Infrared (ATR-FTIR) spectroscopy (Elmer-Perkin) was performed on the GalC7 powder, dried 'stiff' GelMA gel and the corresponding dried composite gel containing self-assembled GalC7 fibres. Both gels were dried for 48 h at room temperature. The scans were produced at a resolution of 4 cm^{-1} between 4000 cm^{-1} and 400 cm^{-1}.

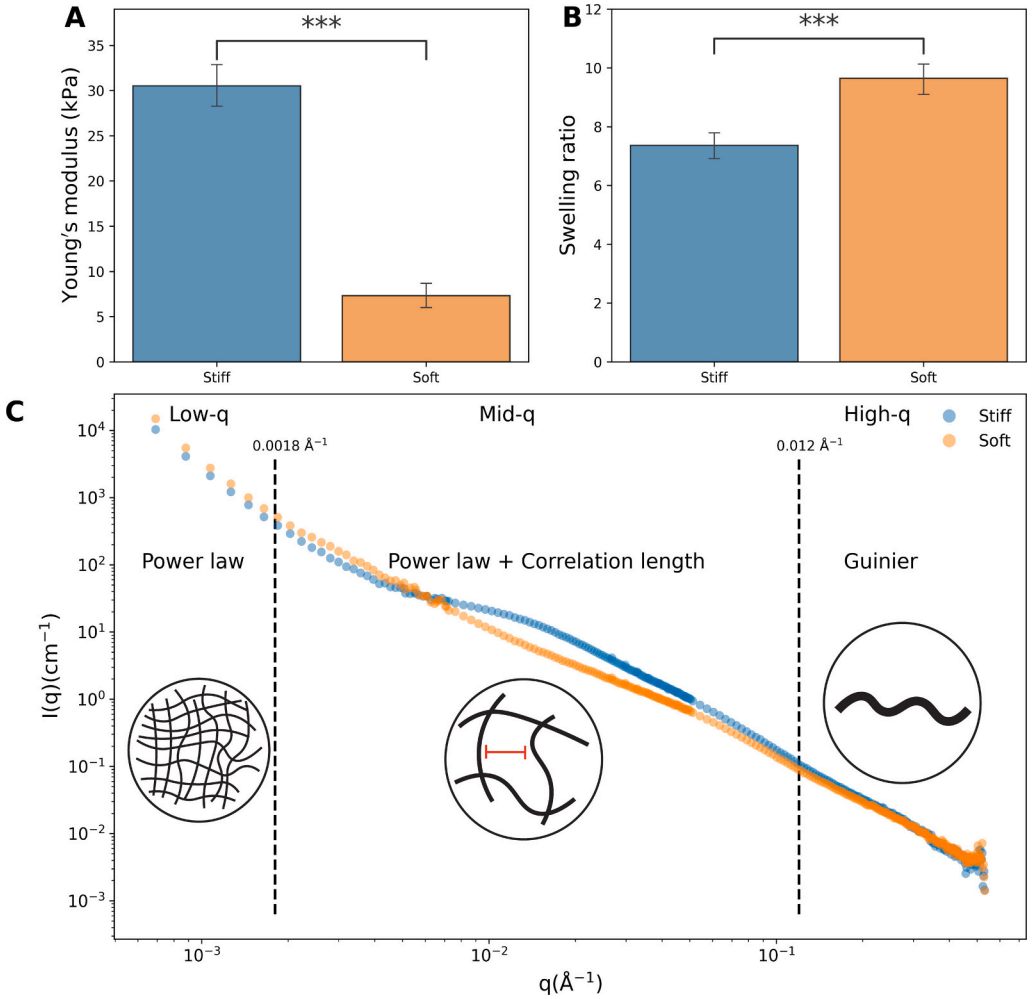

Fig. 2. (A) Young's modulus and (B) Swelling ratio of soft and stiff GelMA hydrogels. The data is displayed as the average from 9 gels per group and 100 force curves per gel. The error bars represent the standard deviation between the gels. Statistical analysis was performed by Welch's t-test, with significance indicated by *** for $p < 0.001$, (C) Full range SANS data for a single soft and stiff GelMA hydrogel with fitting models used for each Q-range indicated.

3. Results and discussion

3.1. Scattering of pure GelMA hydrogels

AFM was performed on GelMA hydrogels (78 % DOF), crosslinked for different amounts of time, to determine their mechanical properties. Force indentation curves performed at the surface of the gels measured the average Young's modulus at 30.5 kPa ± 3.5 kPa for the stiff (4 min crosslinked) gels, and 7.3 kPa ± 2.2 kPa for the soft (1 min crosslinked) (Fig. 2A). This Young's modulus matches that of physiologically soft (<10 kPa) and stiff (>30 kPa) tissue, which has relevance to specific healthy and diseased states of some soft tissues [63]. For example, tissue stiffness increases from ~10 kPa to >50 kPa during cardiac scar formation [22], and 5 kPa to 20–30 kPa during lung cancer [64]. The measured modulus is also in accordance with other reported studies with similar GelMA concentrations [23,65]. The difference in Young's modulus is due to the number of crosslinks formed between adjacent gelatin chains. Gels that are crosslinked for longer periods form a greater amount of crosslinks, resulting in a more rigid and constricted network and, therefore, a greater Young's modulus. The more constricted and rigid matrix also affects the gel's ability to absorb water, as the more rigid network prevents the hydrogel from expanding and swelling. The 4-min crosslinked gels had a significantly lower swelling ratio of 7.4 ± 0.6 compared to that of 1-min crosslinked gels, 9.6 ± 0.7 (Fig. 2B).

SANS and USANS data can be used to probe the structure and arrangement of the gel at different length scales by examining the scattering of the gel across a wide q range. At very low-q (<0.002 $Å^{-1}$) the data provides insight into the overall larger-structural organization of the polymer network. At mid q (0.002 $Å^{-1} > q > 0.1$ $Å^{-1}$), we start to probe scattering at the local network structure, mesh size and interaction between adjacent polymer strands. At high q values q (>0.1 $Å^{-1}$), we start to probe the scattering due to the polymer chains themselves, yielding information about the radius of gyration (average distance of all segments from the centre of mass), these different scattering aspects are summarised in Fig. 2C.

To investigate how the nano and micron structure of the gel changes in relation to crosslinking time/crosslinking density, we interrogated the data as Kratky plots, which provide a measure of a polymer's deviation from an ideal Gaussian coil. When a polymer deviates from the ideal Gaussian behaviour, it is seen as a peak in the Kratky plot [66–68]. Such a peak can be used to identify specific correlation lengths. The collected data for the stiff GelMA hydrogel is compared to the theoretical scattering from an ideal polymer chain in a dilute solution with a radius of gyration of 0.7 nm [69] (supplementary Figs. S1A and B). The differences between the observed scattering of the GelMA hydrogel and the ideal scattering (Debye function) are a direct result of the mesh network and interactions between fibres.

In the Kratky plot (Fig. 3A), peaks appear at 0.016 $Å^{-1}$ and 0.06 $Å^{-1}$ for the stiff GelMA hydrogel, although the peak at 0.06 $Å^{-1}$ is partially hidden by the larger peak at 0.016 $Å^{-1}$. In the soft GelMA hydrogel, only one peak appears at 0.06 $Å^{-1}$. Because of the presence of these two peaks in the stiff GelMA hydrogel, the SANS spectra for the soft and stiff GelMA

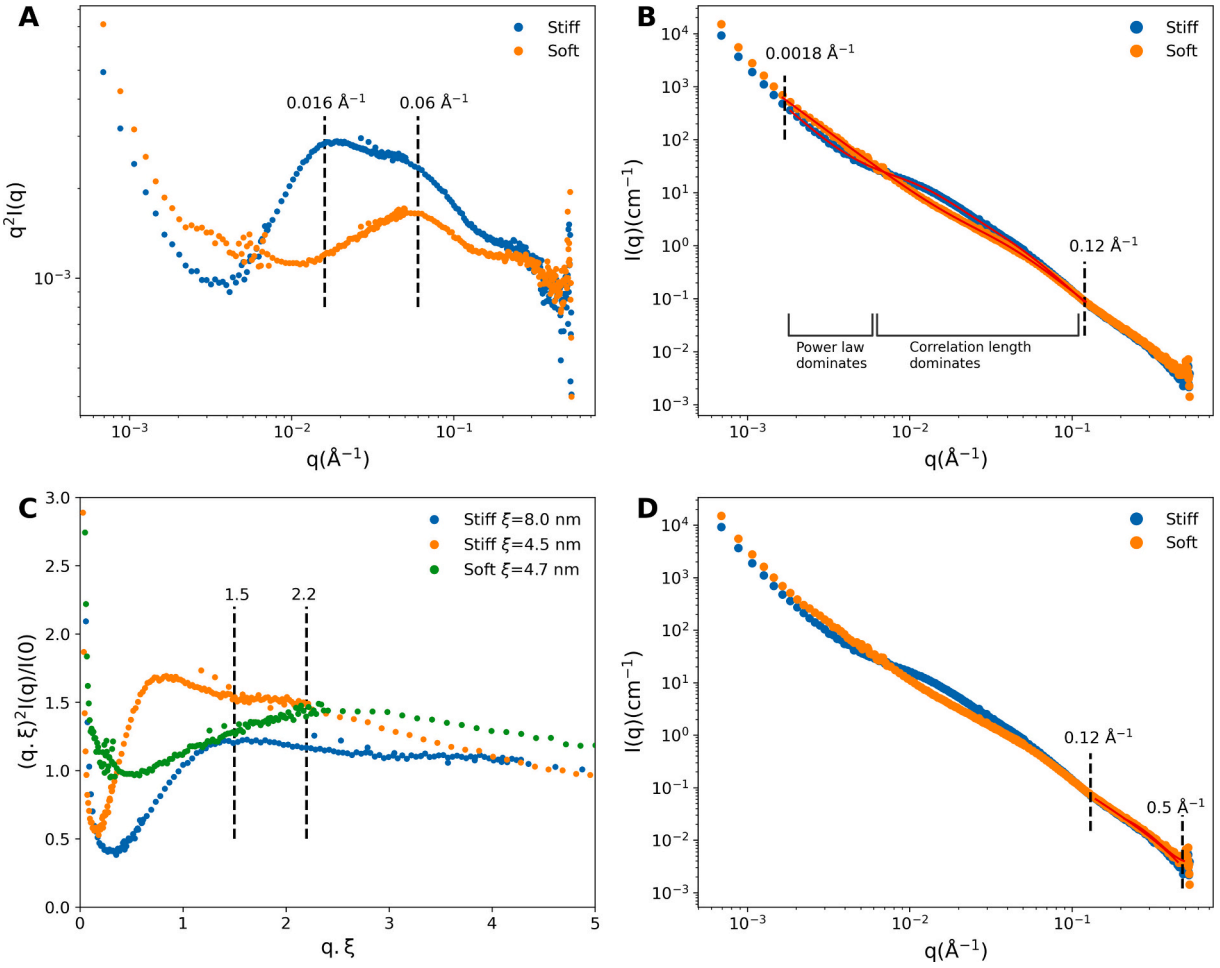

Fig. 3. (A) Kratky plot for a single soft and stiff GelMA hydrogel. (B) SANS data with correlation length model overlaid (Eq. 5) for a single soft and stiff GelMA hydrogel. (C) Dimensionless Kratky plot for a single soft GelMA hydrogel scaled by 4.7 nm and a stiff GelMA hydrogel scaled by 4.5 nm and 8.0 nm. (D) SANS data with Guinier model overlaid (Eq. (6)).

hydrogels were fitted using the power-law + correlation length model with two different correlation length terms in the range of 0.0018 $Å^{-1}$ to 0.12 $Å^{-1}$ (350 nm to 5.2 nm) (Fig. 3B). The correlation length model is particularly useful for characterising hydrogels as it describes the polymer concentration/density in the network and can provide insights into the network porosity/mesh size or any clustering effects [70]. The scattering intensity *I(q)* for the correlation length model is calculated as:

$$I(q) = \frac{A}{q^n} + \frac{B_1}{1 + (q\,\xi_{L1})^{m_1}} + \frac{B_2}{1 + (q\,\xi_{L2})^{m_1}} bkg \quad (5)$$

Where q is the scattering vector, and *bkg* is the incoherent background scattering. The first term (power law) dominates the fit in the lower region of the mid-q domain and describes the power law scattering/ fractal structure of the network at this size scale. The second and third terms are from the Lorentzian function/correlation length model and are used to fit scattering in the higher end of the mid-q range, as indicated in Fig. 3B [70]. ξ is the correlation length, and in most cases, for a polymer network, the correlation length is an indication of the network mesh size/ separation distance between polymers or the size of formed aggregates. A and B are scaling factors for the power law and Lorentzian terms, respectively. Fitting values are summarised in Table 2, and residuals are provided in Supplementary Fig. S1C.

The correlation lengths for the stiff hydrogel were found to be 4.5 nm and 8.0 nm, which represents the two peaks seen in the Kratky plot at 0.016 $Å^{-1}$ and 0.06 $Å^{-1}$. For the soft hydrogel, the correlation lengths were found to be 4.7 nm and 0 nm, which essentially simplifies the model down to only having one correlation length term, which is confirmed by the single peak in the Kratky plot. The dimensionless Kratky plot is scaled by both the correlation length and $I(0)$, the zero-scattering intensity ($q = 0$). $I(0)$ is obtained by plotting the pair inversion function. This plot (Fig. 3C) provides further information on the shape of the scattering structure. Dense aggregates will exert a peak in the dimensionless Kratky plot at $q.\xi_L < 1.73$ ($\sqrt{3}$), which fits the first peak in the stiff hydrogel, when scaled by $\xi_L = 8.0$ nm. This suggests that this peak can be attributed to the formation of small, dense aggregates that are tightly crosslinked. This feature is not present in the soft GelMA scattering data. Mesh size/network features appear as a peak in the dimensionless Kratky plot when $q.\xi_L$ is greater than 2, as is the case for the peak present in the soft GelMA data, and the second peak in the stiff GelMA data, when they are scaled by 4.7 nm and 4.5 nm respectively (both peaks sit at approximately $q.\xi_L = 2.2$).

This interpretation indicates minimal difference between the pore sizes in the soft and stiff hydrogels, with a polymer chain separation in both gels of approximately 4.7 nm and 4.5 nm, respectively. Instead, tightly crosslinked regions are evident within the stiff hydrogel, which appear as aggregates with an approximate size of 8.0 nm. The crosslinking process is a chain polymerization reaction, that occurs without stirring, and it is very likely that it will favour polymerization on a small length scale, leading to small clusters. These cross-linked clusters are assumed to be responsible for the increase in stiffness and a decrease in the overall swelling ratio of the stiff GelMA, without significantly decreasing the size of pores outside the tightly cross-linked areas.

Contrast matching would need to be done to more accurately determine the exact position of the minor peak (0.06 $Å^{-1}$) in the stiff hydrogel, to determine whether there is a significant increase or decrease in the pore size. GelMA is considered relatively homogenous [71], but the introduction of tightly crosslinked areas could cause the stiffness to differ spatially on the nanometre scale, that is too small to be resolved by colloidal AFM. These larger structures and potential spatial inhomogeneities in stiffness could cause differences in cell responses depending on whether or not a cell is bound to the highly crosslinked aggregates.

Extending the correlation length model + power law over the entire SANS spectra results in significantly larger residuals in both the high-q and low-q domains (Supplementary Fig. S1C), necessitating the use of other models to describe these length scales. Deviation from the correlation length model in the high-q range is due to scattering of the individual fibres themselves [80]. The Guinier's approximation [81] can be used to measure the core radius of the polymer chains, and was used to fit the data above 0.12 $Å^{-1}$. The Guinier model is as follows:

$$I(q) = I(0)\exp\left(-\frac{q^2 R_g^2}{3}\right) \quad (6)$$

where R_g is the radius of gyration of the polymer, which represents the effective size of the scattering "particle", and I(0) is the intensity at zero scattering ($q = 0$). R_g of the stiff and soft hydrogels are calculated as 0.52 nm and 0.51 nm, respectively (the fit is shown in Fig. 3D), residuals for the Guinier approximation are given in Supplementary Fig. S1D. This translates to a fibre thickness of 0.73 nm and 0.72 nm (core radius $R_C = \sqrt{2}.R_g$ [82]), for the stiff and soft hydrogels, respectively.

The fit deviates from the correlation model in the low-q region due to scattering of the continuous network as a whole [83]. A power law can reveal information on the compactness of the polymer segments and the fractal dimension of the gel. To determine this, a power law approximation was fitted to the USANS data (fit and residuals are given in Supplementary Fig. S1E and F) as follows:

$$I(q) = \frac{A}{q^d} + bkg \quad (7)$$

where d is the power law exponent and A is a scaling factor. The power law exponent (d) in the low-q ($<1.8 \times 10^{-3}$ $Å^{-1}$/>350 nm) domain describes the arrangement of the mesh network at a larger scale. Stiff hydrogels have an exponent of 3.07 ± 0.05, while soft gels have an exponent of 2.65 ± 0.06. This indicates that, at larger scales, the stiff hydrogel has a sharper interface, exhibiting fractal scattering surface with a rough surface, which would indicate that the stiff gels have more branched connections and a denser network compared with the soft hydrogel, which scatters as a mass fractal but with collapsed polymer chains [84]. Fits and residuals are provided in Supplementary Figs. S1E and F.

Taken together, our SANS and USANS data demonstrate a GelMA network, where the overall pore size does not appear to change much with crosslinking density, but where tightly crosslinked aggregates appear for the stiff gels, with higher crosslinking density. Fig. 4 illustrates the possible polymer network structure, based on the scattering data from the soft and stiff GelMA hydrogels.

The GelMA network structure at different Young's moduli has previously been characterised using SEM, leading to vast overestimation of the pore size, reported as 24 μm(4.5 kPa) [72], 26 μm (27 kPa) [73], and as high as 190 μm [74]. It has also been reported using SEM that the pore size of the GelMA hydrogels decreased as the Young's modulus/crosslinking density increases, 77 μm at 5.2 kPa to 26 μm at 27 kPa [73]. There are no previous reports of the tightly crosslinked aggregates that we report here, in stiff GelMA hydrogels. This may be due to the stringent sample preparation (freezing or freeze-drying) required for SEM or

Table 2
Fitting parameters for soft and stiff pure GelMA hydrogels, determined from 2 separate samples for stiff hydrogels and a single soft hydrogel (apart from the USANS d exponent, which is derived from data from 2 samples for both soft and stiff gels).

Sample	R_C (nm)	ξ_1 (nm)	m_1	B_1	ξ_2 (nm)
Stiff	0.73 ± 0.01	4.5 ± 0.1	2.84 ± 0.1	1.5	8.0 ± 0.2
Soft	0.72	4.7	2.27	0.9	0

	m_2	B_2	n	d (low-q USANS)
Stiff	3.1 ± 0.05	17.3 ± 0.2	2.8 ± 0.1	3.07 ± 0.05
Soft	0	0	2.3	2.65 ± 0.06

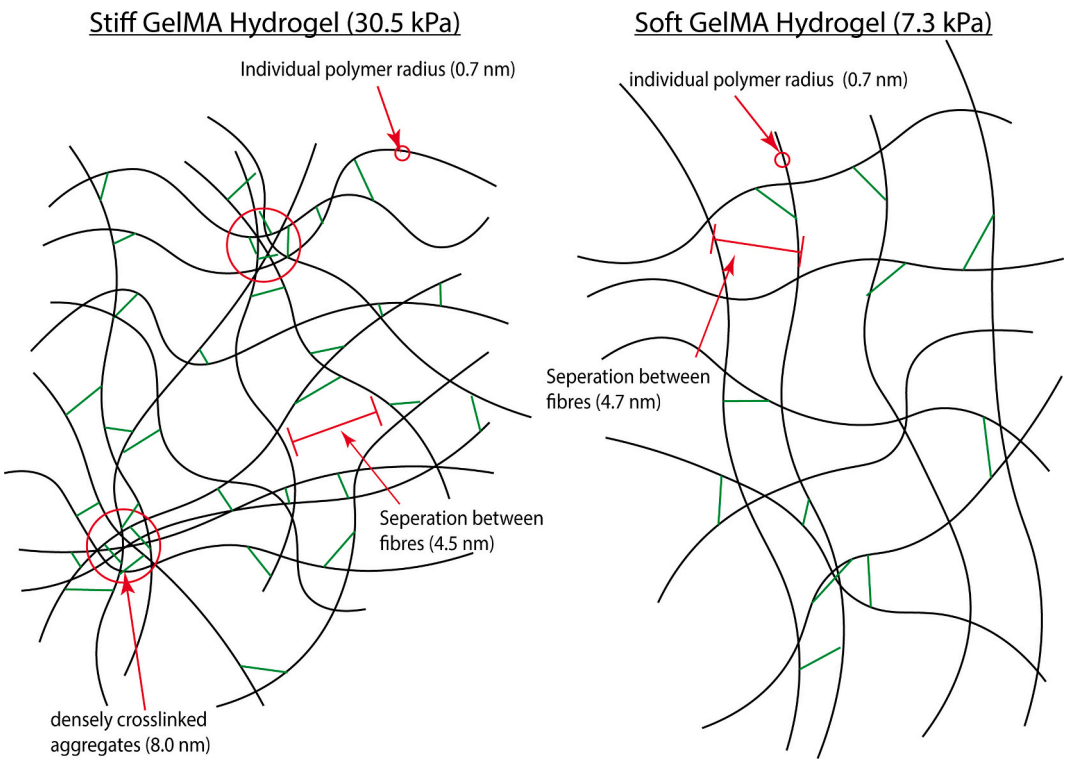

Fig. 4. Illustration/interpretation of the polymer network for stiff and soft GelMA hydrogels based on SANS scattering data.

cryo-SEM, which causes significant changes to the GelMA structure. This highlights the benefit of performing SANS on polymer hydrogels to characterise the network structure. SANS and USANS have previously been used to characterise how the network structure changes as the hydrogels' Young's modulus increases for different hydrogel systems. For example, alginate hydrogels have been previously studied with SANS [75–77]. Alginate gels enriched with glucose showed an increase in inhomogeneities/aggregates with the addition of glucose, up to an aggregate size of 46.5 nm at 45 wt% glucose from 32.0 nm when no glucose was added [76]. This was accompanied by an increase in compressive modulus as the glucose concentration increased [76]. Conversely, SANS showed that increasing crosslinking density of hyaluronic acid-based hydrogels resulted in a reduction in the mesh size from 223 nm to 93 nm [78]. In crosslinked poly(ethylene glycol) (PEG)

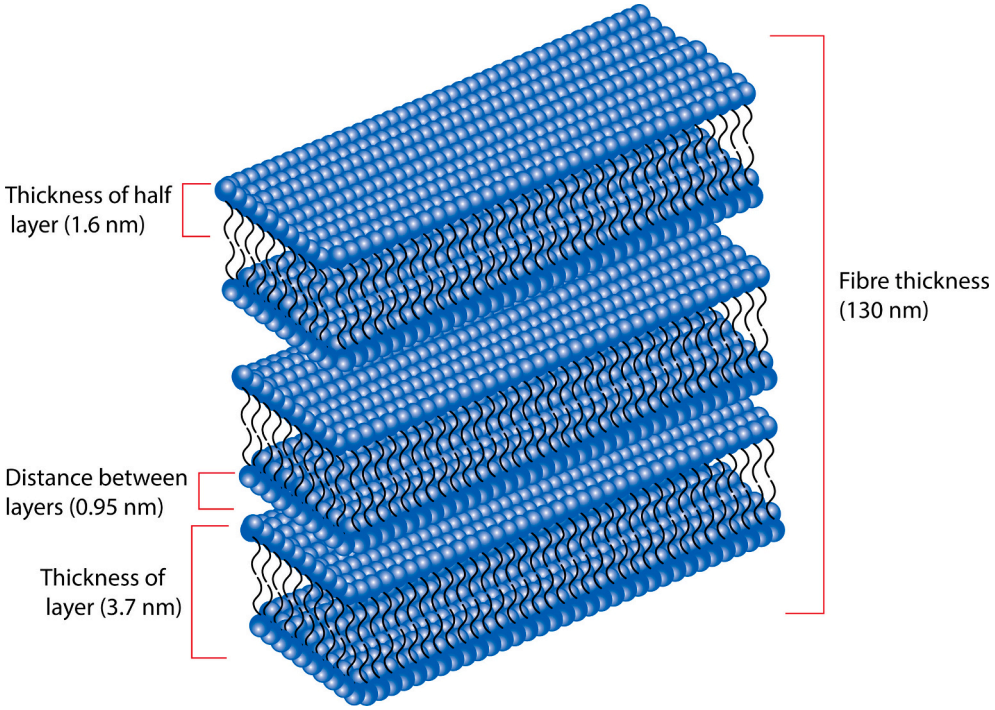

Fig. 5. Illustration of GalC7 fibres with dimensions based on SANS data and SAXS data from [56].

hydrogels, higher molecular weight PEGs formed more homogenous networks while lower molecular weight PEG led to the formation of aggregates [79]. Whether the pore size decreases or the formation of aggregates occurs as the crosslinking density increases may depend on the concentration and polymer used.

3.2. Scattering of GalC7 gels

GalC7 are amphiphilic molecules that readily self-assemble into fibres, which create hydrogels [24]. The supramolecular fibres are made up of repeating bilayers of GalC7, stacked on top of each other, these fibres are depicted in Fig. 5. Scattering from the GalC7 fibres can give information about the shape and dimensions associated with the size and stacking of the fibres.

Neutron scattering data (Fig. 6) from pure GalC7 gels were fitted to the Gunier-Porod model (<0.12 Å^{-1}/>5.2 nm), to determine the radius of gyration of the fibre. The Guinier-Porod model used is as follows [82].

$$I(Q) = \frac{G}{q^s}\exp\left(\frac{-q^2R_g^2}{3-s}\right) \text{ for } q \le q_1 \tag{8}$$

$$I(Q) = \frac{D}{q^d}\ q \ge q_1 \tag{9}$$

where R_g is the radius of gyration, d is the Porod exponent, G and D are scaling factors, q_1 is the q-value at which the model switches from Eq. (8) to Eq. (9) and s is the shape form factor, which helps model nonspherical objects. For globular objects, such as spheres, s has a value of 0, for rods s = 1, and for lamellae or platelets s = 2. Applying continuity of the Guinier and Porod functions and their derivatives yields:

$$q_1 = \frac{1}{R_g}\left[\frac{(d-s)(3-s)}{2}\right]^{\frac{1}{2}} \tag{10}$$

$$D = G\exp\left(-\frac{q_1^2R_g^2}{3-s}\right)q_1^{d-s} \tag{11}$$

Scattering data presented in Fig. 6 can be fitted with a Porod exponent (d) of 4.0 in the mid q region (q = 0.05–0.03 Å^{-1}), which represents a sharp smooth interface with good phase separation between the fibres and the solvent. The shape form factor has a value of 2, representing a lamella structure. R_g has a value of 371 Å, which translates to a fibre thickness of 130 nm (Thickness = $\sqrt{12}.R_g$ [82]), which is comparable to another study which measured the thickness using SEM [24]. Fitting values are summarised in Table 3.

The theoretical size of a single GalC7 molecule can be estimated to 1.65 nm, assuming the bond between carbon atoms amounts to 1.5 Å, the galactose head 5 Å and the amide group 2 Å. There is a sharp peak at 0.40 Å^{-1}/1.6 nm, which can be seen in both the scattering intensity plot (Fig. 6) and the Kratky plot (Supplementary Fig. S2A). This peak is most likely due to scattering from individual GalC7 molecular leaflets (half a bilayer). The pronounced peak at 0.17 Å^{-1} /3.7 nm, in turn, can be attributed to scattering originating from the GalC7 bilayers that stack together to make up GalC7 fibres. The prominence/sharpness of this peak at 3.7 nm shows the predictable and repeatable nature of the bilayer formation. Residuals from the fitted Gunier-Porod model are provided in supplementary Fig. S2B.

Small-angle X-ray scattering (SAXS), which often has a higher resolution than SANS at smaller length scales [85], has previously been performed on GalC7 fibres [50]. The data showed peaks at 3.8 nm, 1.8 nm, and 0.92 nm. This correlates with peaks in our dataset of a single GalC7 bilayer thickness (3.7 nm) and the size of a single molecule/thickness of half a single lamellar (1.8 nm). The additional peak not seen in our SANS data, due to restrictions in the maximum q value attainable, at 0.92 nm, was not identified by the authors but may be attributed to the spacing between stacked lamellae. In the study by Chalard et al. [24], the fibre thickness was also measured by cryo-SEM and SAXS, and was found to be 150 nm ± 100 nm, and 230 nm ± 50 nm, for cryo-SEM and SAXS, respectively. The discrepancy in the measured SAXS value for fibre thickness may be in part due to the limitations of SAXS at higher length scales. Optical microscopy has previously revealed that formed GalC7 fibres can extend beyond 500 μm in length [50].

It was not possible to extract length or width dimensions of the GalC7 fibres from our SANS or USANS data (section 2.3), despite the existence of three or four Guinier region models that have been established to quantify the width and length of lamellar structures [82]. This can be due to both the width and length exceeding the size range of SANS/USANS, or the scattering resulting from interaction/separation between

Table 3
Fitting values for GalC7 fibres. All presented parameters are average values with standard deviation from fitting scattering data from three independent samples.

Sample	*Rg* (nm)	*d*	*s*
GalC7	37.1 ± 0.2	4.0 ± 0.1	2 ± 0.05

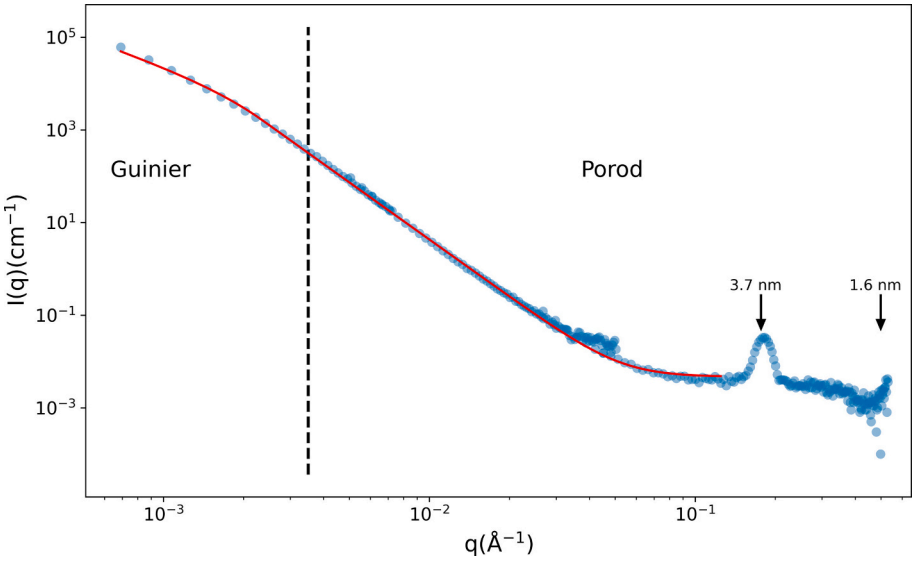

Fig. 6. SANS scattering data for a gel of pure GalC7 fibres with Gunier-Porod model overlaid (Eq. 8 and 9) for values <0.1 Å^{-1}/>6.3 nm.

fibres hides the scattering due to the length or the width.

3.3. Scattering of composite hydrogels

Combining GelMA with the much larger supramolecular fibres creates composite gels where the supramolecular fibres reinforce the GelMA gels, and where they can act as initial guidance to cells. Over time, the fibres have been found to disassemble, leaving pores within the GelMA for cells to interact with [24]. While we have previously shown that these composite gels can be fabricated [24], it is important to characterise any interaction between the GelMA and the GalC7 fibres, and whether the GalC7 fibres disrupt the GelMA network, which can be probed using neutron scattering.

To understand if there are any interactions between the GelMA and the GalC7 fibres, the scattering of the composite (GelMA + GalC7) hydrogels was compared with the individual GalC7 fibre and the GelMA scattering curves (Fig. 7A and B). The composite gel scattering was also compared to the summation of the GalC7 and GelMA scattering data (Fig. 7C and D), which is produced by adding the scattering intensity of the individual stiff GelMA and GalC7 fibres scattering data.

From Fig. 7A and B, it is seen that the scattering of the composite hydrogels is dominated by the large GalC7 fibres in the low-q range (<0.007 Å^{-1}), while GelMA scattering dominates in the high-q range (>0.007 Å). In the high-q range, GelMA appears to significantly suppress the peak at 0.17 Å^{-1} seen in the GalC7 curve (A and B), although it is still faintly present in the composite curve. This suppression could be due to poor contrast between the GelMA and the GalC7 layers. It is also important to note that while the pure GalC7 fibres were produced in D_2O, GelMA and the composite gels were made in H_2O, dried and swollen in D_2O. It is therefore possible that there is residual H_2O associated with the hydrophilic GalC7 heads in the composite gels, which would reduce the contrast further. The scattering length density of H_2O (-0.55×10^{-6} Å^{-2}) is much closer to that of the GalC7 molecules (0.54×10^{-6} Å^{-2}) than that of D_2O (6.35×10^{-6} Å^{-2}).

Some differences are seen in the Kratky plot (Fig. 7D) between the summation of the GalC7 and GelMA curves and the composite gels. The composite gels have a slight increase in intensity between 0.1 Å^{-1} to 0.007 Å^{-1}, which would indicate some increase in the concentration of pores and formed aggregates. Though GelMA concentration remains the same between the composite and pure GelMA gels, there may be a slight decrease in swelling ratio due to the presence of the fibres or improper swelling, due to the shorter time spent hydrated before scattering. Since there is no shift of the curves to higher or lower q-values, only a small change in scattering intensity, it would indicate there is minimal disruption of the GelMA network from the GalC7 fibres. It was also previously shown that these composite hydrogels did not show any difference in Young's modulus compared with pure GelMA hydrogels at the same crosslinking time when measured by AFM [24]. Due to the small indentation depth of AFM, it would only measure the local properties of the surface GelMA, which would further support the interpretation that the stiffness and network properties don't change due to the presence of the GalC7 fibres.

There are also small differences in the composite and GelMA + GalC7 summation curves, when q is less than 0.007 Å^{-1}, where the GalC7 fibres

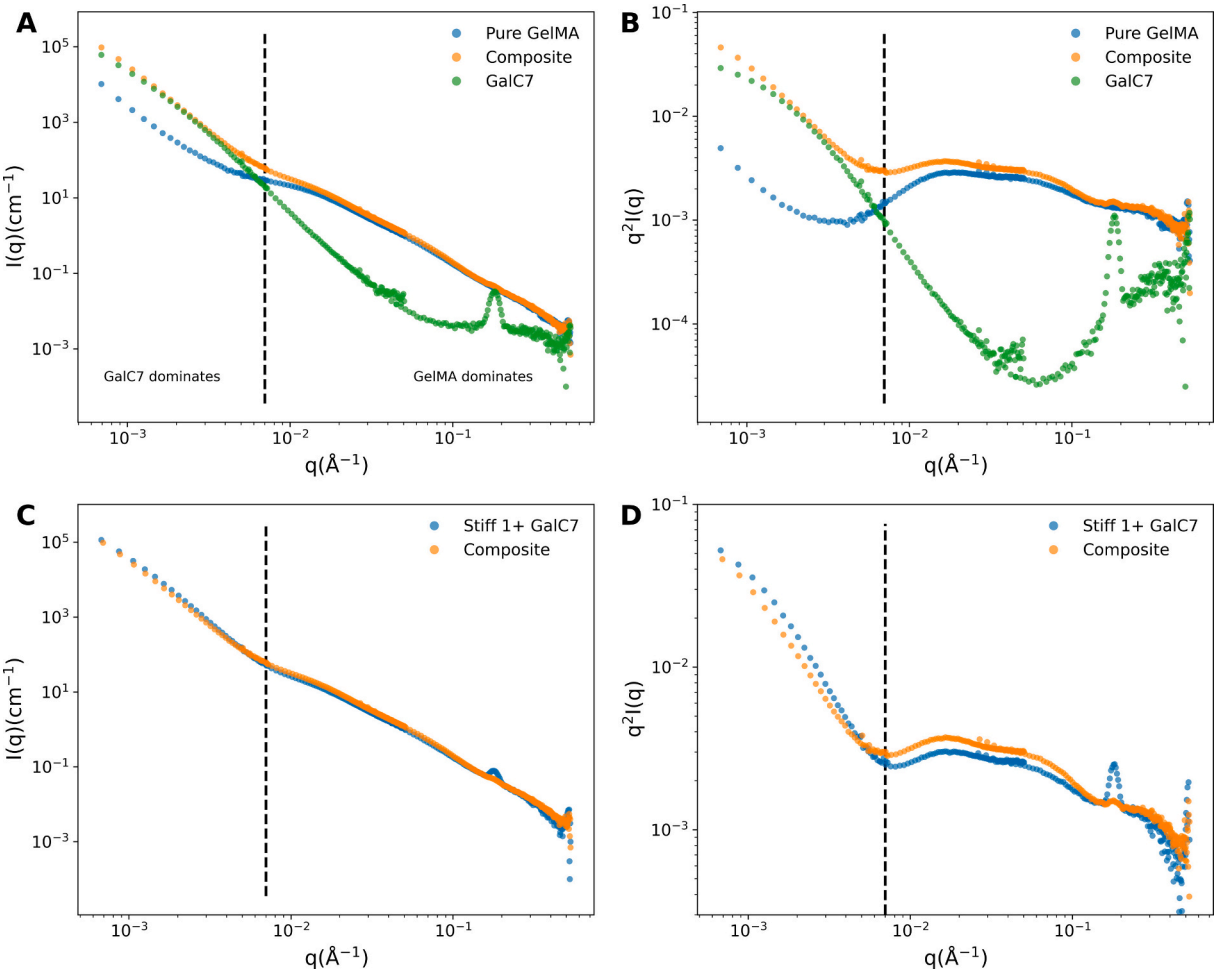

Fig. 7. (A) SANS data and (B) Kratky plot, of pure GelMA, pure GalC7 and composite hydrogels (C) SANS data and (D) Kratky plot, of Composite hydrogel and the Stiff 1 + GalC7 which is the summation of the two curves Pure GelMA and GalC7 in A and B.

dominate. The scattering curve of the composite hydrogels is slightly shifted towards lower q values in this region, which may indicate that the composite gels have slightly thicker fibres. Such small differences may be due to using different cooling rates during sample preparation, for composite and GalC7 samples (3 h for composites compared to 20 min for GalC7 fibres), which is known to cause differences in fibre growth, with shorter and thinner fibres produced at higher cooling rates [24]. These inconsistencies occurred as the pure GalC7 gels do not tolerate drying and were prepared using D_2O onsite at ANSTO, while the composite gels were prepared using H_2O at the University of Auckland. Also, the self-assembly, like crystallization, is sensitive to the local concentration and diffusion of the GalC7 free molecules around the formed fibres, which could be rather different in the presence or absence of the GelMA in the solution.

FTIR was performed on the GalC7 powder, dried 'stiff' GelMA gel and the corresponding dried composite gel containing self-assembled GalC7 fibres (supplementary Fig. S3). The composite gel FTIR is almost identical to the GelMA spectra, due to the low concentration of GalC7 in the gel (22 times more GelMA weight compared to GalC7). The near identical FTIR confirms that the GalC7 fibres do not alter the chemical structure of the GelMA gel.

USANS was also performed on the composite hydrogels after being swelled for 1 h, data is given in supplementary fig. S2D and was fitted to the power law equation (Eq. 7) (supplementary Fig. S4). Composite gels had a power law exponent of 2.8 ± 0.1, which indicates the GalC7 fibres scatter as a mass fractal within the gel.

4. Conclusion

This work provides a detailed analysis of two different GelMA-based hydrogel systems, pure GelMA with the same polymer concentration but different crosslinking, and composite GelMA/GalC7 gels. The data from pure GelMA hydrogels demonstrated that an increase in Young's modulus did not significantly decrease the size of the majority of pores/separation between fibres. Stiffer hydrogels were, however, observed to have areas of tightly crosslinked particle-like bundles, which results in the matrix being more constrained, explaining the higher Young's modulus and lower swelling ratio. This study furthermore provides insights into the structural details of supramolecular GalC7 fibre gels and the composite GalC7-GelMA hydrogels. The data confirms expected fibre dimensions and bilayer structure of GalC7 fibres and adds insight that these GalC7 fibres have very little interaction with the surrounding GelMA hydrogel, which highlights the fact that the supramolecular assembly of GalC7, which follows the same mechanism as a crystallization phenomenon, is not really disturbed by the presence of GelMA as a solute. Characterising structures and interaction of highly used materials in the field of tissue engineering may facilitate understanding of cell interaction and phenotype and help drive advancements in tissue engineering.

CRediT authorship contribution statement

Harrison Porritt: Writing – original draft, Visualization, Validation, Methodology, Investigation, Formal analysis. **Anaïs Chalard:** Writing – review & editing, Methodology, Conceptualization. **Juliette Fitremann:** Writing – review & editing, Conceptualization. **Jitendra Mata:** Writing – review & editing, Methodology, Formal analysis, Data curation. **Jenny Malmström:** Writing – review & editing, Supervision, Resources, Methodology, Investigation, Conceptualization.

Declaration of Generative AI and AI-assisted technologies in the writing process

During the preparation of this work the author(s) used Microsoft copilot in order to edit and review writing. After using this tool/service, the author(s) reviewed and edited the content as needed and take(s) full responsibility for the content of the publication.

Declaration of competing interest

The authors declare the following financial interests/personal relationships which may be considered as potential competing interests: J. Fitremann can receive royalties from the selling of N-heptyl-D-galactonamide by the company Innov'Orga (France). These royalties expected would represent very low amounts and in any case they will not influence her scientific statements related to with this molecule. If there are other authors, they declare that they have no known competing financial interests or personal relationships that could have appeared to influence the work reported in this paper.

Acknowledgements

We acknowledge the support of the ANSTO, in providing the small angle neutron scattering facilities (Quokka) and ultra small angle neutron scattering facilities (Kookaburra) (Proposal number P17939). Financial support is acknowledged from the Faculty of Engineering and design at the University of Auckland, the MacDiarmid Institute for Advanced Materials and Nanotechnology and the Royal Society Te Apārangi (Rutherdord Discovery Fellowship). Harrison Porritt also acknowledges support from the University of Auckland, in the form of an Auckland University Doctoral Scholarship.

Appendix A. Supplementary data

Supplementary data to this article can be found online at https://doi.org/10.1016/j.jcis.2025.138443.

Data availability

Data will be made available on request.

References

[1] T. Weigel, et al., Fully synthetic 3D fibrous scaffolds for stromal tissues—replacement of animal-derived scaffold materials demonstrated by multilayered skin, Adv. Mater. 34 (10) (2022) 2106780, https://doi.org/10.1002/adma.202106780.
[2] A.A. Solbu, et al., Assessing cell migration in hydrogels: an overview of relevant materials and methods, Mater. Today Bio 18 (2023) 100537, https://doi.org/10.1016/j.mtbio.2022.100537.
[3] K.L. Xu, et al., Microinterfaces in biopolymer-based bicontinuous hydrogels guide rapid 3D cell migration, Nat. Commun. 15 (1) (2024) 2766, https://doi.org/10.1038/s41467-024-46774-y.
[4] I.M. Savić Gajić, I.M. Savić, Z. Svirčev, Preparation and characterization of alginate hydrogels with high water-retaining capacity, Polymers 15 (12) (2023) 2592, https://doi.org/10.3390/polym15122592.
[5] E.E. Antoine, P.P. Vlachos, M.N. Rylander, Review of collagen I hydrogels for bioengineered tissue microenvironments: characterization of mechanics, structure, and transport, Tissue Eng. Part B Rev. 20 (6) (2014) 683–696, https://doi.org/10.1089/ten.teb.2014.0086.
[6] E. Larrañeta, M. Henry, N.J. Irwin, J. Trotter, A.A. Perminova, R.F. Donnelly, Synthesis and characterization of hyaluronic acid hydrogels crosslinked using a solvent-free process for potential biomedical applications, Carbohydr. Polym. 181 (2018) 1194–1205, https://doi.org/10.1016/j.carbpol.2017.12.015.
[7] S. Sun, et al., Drug delivery systems based on polyethylene glycol hydrogels for enhanced bone regeneration, Front. Bioeng. Biotechnol. 11 (2023) 1117647, https://doi.org/10.3389/fbioe.2023.1117647.
[8] B. Díaz-Bello, et al., Method for the direct fabrication of polyacrylamide hydrogels with controlled stiffness in polystyrene multiwell plates for mechanobiology assays, ACS Biomater Sci. Eng. 5 (9) (2019) 4219–4227, https://doi.org/10.1021/acsbiomaterials.9b00988.
[9] Y. Xing, B. Varghese, Z. Ling, A.S. Kar, E. Reinoso Jacome, X. Ren, Extracellular matrix by design: native biomaterial fabrication and functionalization to boost tissue regeneration, Regen. Eng. Transl. Med. 8 (1) (2022) 55–74, https://doi.org/10.1007/s40883-021-00210-5.
[10] S.K. Asl, M. Rahimzadegan, A.K. Asl, Progress in cardiac tissue engineering and regeneration: implications of gelatin-based hybrid scaffolds, Int. J. Biol. Macromol. 261 (2024) 129924, https://doi.org/10.1016/j.ijbiomac.2024.129924.
[11] Y.-H. Kim, S. Vijayavenkataraman, G. Cidonio, Biomaterials and scaffolds for tissue engineering and regenerative medicine, *BMC* Methods 1 (1) (2024) 2, https://doi.org/10.1186/s44330-024-00002-7.

[12] C.M. Jeffries, et al., Small-angle X-ray and neutron scattering, Nat. Rev. Methods Primers 1 (1) (2021) 70, https://doi.org/10.1038/s43586-021-00064-9.

[13] J.L. Whittaker, et al., Structural evolution of photocrosslinked silk fibroin and silk fibroin-based hybrid hydrogels: a small angle and ultra-small angle scattering investigation, Int. J. Biol. Macromol. 114 (2018) 998–1007, https://doi.org/10.1016/j.ijbiomac.2018.03.044.

[14] M. Shibayama, Small angle neutron scattering on gels, in: R. Borsali, R. Pecora (Eds.), Soft Matter Characterization, Springer Netherlands, Dordrecht, 2008, pp. 783–832, https://doi.org/10.1007/978-1-4020-4465-6_14.

[15] C. Maibohm, A. Saldana-Lopez, O.F. Silvestre, J.B. Nieder, 3D polymer architectures for the identification of optimal dimensions for cellular growth of 3D cellular models, Polymers (Basel) 14 (19) (2022) 4168, https://doi.org/10.3390/polym14194168.

[16] M. Asadikorayem, L.G. Brunel, P. Weber, S.C. Heilshorn, M. Zenobi-Wong, Porosity dominates over microgel stiffness for promoting chondrogenesis in zwitterionic granular hydrogels, Biomater. Sci. (2024), https://doi.org/10.1039/D4BM00233D.

[17] J. Gu, Y. Zhao, Y. Guan, Y. Zhang, Effect of particle size in a colloidal hydrogel scaffold for 3D cell culture, Colloids Surf. B Biointerfaces 136 (2015) 1139–1147, https://doi.org/10.1016/j.colsurfb.2015.11.021.

[18] S.-N. Park, J.-C. Park, H.O. Kim, M.J. Song, H. Suh, Characterization of porous collagen/hyaluronic acid scaffold modified by 1-ethyl-3-(3-dimethylaminopropyl) carbodiimide cross-linking, Biomaterials 23 (4) (2002) 1205–1212, https://doi.org/10.1016/S0142-9612(01)00235-6.

[19] M. Koch, M.K. Włodarczyk-Biegun, Faithful scanning electron microscopic (SEM) visualization of 3D printed alginate-based scaffolds, Bioprinting 20 (2020) e00098, https://doi.org/10.1016/j.bprint.2020.e00098.

[20] L.L. Kuleshova, S.S. Gouk, D.W. Hutmacher, Vitrification as a prospect for cryopreservation of tissue-engineered constructs, Biomaterials 28 (9) (2007) 1585–1596, https://doi.org/10.1016/j.biomaterials.2006.11.047.

[21] S. Tavukcuoglu, T. Al-Azawi, A.A. Khaki, S. Al-Hasani, Is vitrification standard method of cryopreservation, Middle East Fertil. Soc. J. 17 (3) (2012) 152–156, https://doi.org/10.1016/j.mefs.2012.07.007.

[22] A. Franco, B. Van Durme, S. Van Vlierberghe, C. Dupont-Gillain, Misleading pore size measurements in gelatin and alginate hydrogels revealed by confocal microscopy, Tissue Eng. Part C Methods 30 (7) (2024) 307–313, https://doi.org/10.1089/ten.tec.2024.0117.

[23] A.E. Chalard, A.W. Dixon, A.J. Taberner, J. Malmström, Visible-light stiffness patterning of GelMA hydrogels towards in vitro scar tissue models, Front. Cell Dev. Biol. 10 (2022) 946754, https://doi.org/10.3389/fcell.2022.946754.

[24] A.E. Chalard, et al., Dynamic composite hydrogels of gelatin methacryloyl (GelMA) with supramolecular fibers for tissue engineering applications, Biomater. Adv. 163 (2024) 213957, https://doi.org/10.1016/j.bioadv.2024.213957.

[25] K.L. Miller, et al., Rapid 3D BioPrinting of a human iPSC-derived cardiac micro-tissue for high-throughput drug testing, Organs-on-a-Chip 3 (2021) 100007, https://doi.org/10.1016/j.ooc.2021.100007.

[26] D. Loessner, et al., Functionalization, preparation and use of cell-laden gelatin methacryloyl–based hydrogels as modular tissue culture platforms, Nat. Protoc. 11 (4) (2016) 727–746, https://doi.org/10.1038/nprot.2016.037.

[27] K.S. Lim, et al., Visible light cross-linking of gelatin hydrogels offers an enhanced cell microenvironment with improved light penetration depth, Macromol. Biosci. 19 (6) (2019) 1900098, https://doi.org/10.1002/mabi.201900098.

[28] S. Bupphathong, C. Quiroz, W. Huang, P.-F. Chung, H.-Y. Tao, C.-H. Lin, Gelatin methacrylate hydrogel for tissue engineering applications—a review on material modifications, Pharmaceuticals 15 (2) (2022) 171, https://doi.org/10.3390/ph15020171.

[29] T. Nguyen, K.E. Watkins, V. Kishore, Photochemically crosslinked cell-laden methacrylated collagen hydrogels with high cell viability and functionality, J. Biomed. Mater. Res. 107 (7) (2019) 1541–1550, https://doi.org/10.1002/jbm.a.36668.

[30] A.K. Nguyen, P.L. Goering, R.K. Elespuru, S. Sarkar Das, R.J. Narayan, The photoinitiator lithium phenyl (2,4,6-trimethylbenzoyl) phosphinate with exposure to 405 nm light is cytotoxic to mammalian cells but not mutagenic in bacterial reverse mutation assays, Polymers 12 (7) (2020) 1489, https://doi.org/10.3390/polym12071489.

[31] D. Zhao, et al., Effect of altering photocrosslinking conditions on the physical properties of alginate gels and the survival of photoencapsulated cells, Polym. Degrad. Stab. 179 (2020) 109297, https://doi.org/10.1016/j.polymdegradstab.2020.109297.

[32] K.S. Lim, et al., New visible-light photoinitiating system for improved print fidelity in gelatin-based bioinks, ACS Biomater Sci. Eng. 2 (10) (2016) 1752–1762, https://doi.org/10.1021/acsbiomaterials.6b00149.

[33] M.C. Murphy, et al., Regional brain stiffness changes across the Alzheimer's disease spectrum, NeuroImage: Clin. 10 (2016) 283–290, https://doi.org/10.1016/j.nicl.2015.12.007.

[34] J. Song, X. Zeng, C. Li, H. Yin, S. Mao, D. Ren, Alteration in cartilage matrix stiffness as an indicator and modulator of osteoarthritis, Biosci. Rep. 44 (1) (2024) BSR20231730, https://doi.org/10.1042/BSR20231730.

[35] C.O. Heras-Bautista, et al., Cardiomyocytes facing fibrotic conditions re-express extracellular matrix transcripts, Acta Biomater. 89 (2019) 180–192, https://doi.org/10.1016/j.actbio.2019.03.017.

[36] R. Gauvin, et al., Microfabrication of complex porous tissue engineering scaffolds using 3D projection stereolithography, Biomaterials 33 (15) (2012) 3824–3834, https://doi.org/10.1016/j.biomaterials.2012.01.048.

[37] J.W. Seo, G.M. Kim, Y. Choi, J.M. Cha, H. Bae, Improving printability of digital-light-processing 3D bioprinting via photoabsorber pigment adjustment, IJMS 23 (10) (2022) 5428, https://doi.org/10.3390/ijms23105428.

[38] K.A. Mosiewicz, L. Kolb, A.J. van der Vlies, M.P. Lutolf, Microscale patterning of hydrogel stiffness through light-triggered uncaging of thiols, Biomater. Sci. 2 (11) (2014) 1640–1651, https://doi.org/10.1039/C4BM00262H.

[39] K. Yu, et al., Printability during projection-based 3D bioprinting, Bioact. Mater. 11 (2022) 254–267, https://doi.org/10.1016/j.bioactmat.2021.09.021.

[40] L.S.S.M. Magalhães, et al., Printing 3D hydrogel structures employing low-cost stereolithography technology, JFB 11 (1) (2020) 12, https://doi.org/10.3390/jfb11010012.

[41] Y. Wu, et al., The combined effect of substrate stiffness and surface topography on chondrogenic differentiation of mesenchymal stem cells, Tissue Eng. Part A 23 (1–2) (2017) 43–54, https://doi.org/10.1089/ten.tea.2016.0123.

[42] M. Sarem, et al., Interplay between stiffness and degradation of architectured gelatin hydrogels leads to differential modulation of chondrogenesis in vitro and in vivo, Acta Biomater. 69 (2018) 83–94, https://doi.org/10.1016/j.actbio.2018.01.025.

[43] Q. Feng, et al., Engineering the cellular mechanical microenvironment to regulate stem cell chondrogenesis: insights from a microgel model, Acta Biomater. 113 (2020) 393–406, https://doi.org/10.1016/j.actbio.2020.06.046.

[44] C.D. Davidson, et al., Myofibroblast activation in synthetic fibrous matrices composed of dextran vinyl sulfone, Acta Biomater. 105 (2020) 78–86, https://doi.org/10.1016/j.actbio.2020.01.009.

[45] H. Wang, S.M. Haeger, A.M. Kloxin, L.A. Leinwand, K.S. Anseth, Redirecting valvular myofibroblasts into dormant fibroblasts through light-mediated reduction in substrate modulus, PloS One 7 (7) (2012) e39969, https://doi.org/10.1371/journal.pone.0039969.

[46] A.K. Schroer, W.D. Merryman, Mechanobiology of myofibroblast adhesion in fibrotic cardiac disease, J. Cell Sci. 128 (10) (2015) 1865–1875, https://doi.org/10.1242/jcs.162891.

[47] S. Zhang, D. Yan, L. Zhao, J. Lin, Composite fibrous membrane comprising PLA and PCL fibers for biomedical application, Compos. Commun. 34 (2022) 101268, https://doi.org/10.1016/j.coco.2022.101268.

[48] K.A.G. Katsogiannis, G.T. Vladisavljević, S. Georgiadou, Porous electrospun polycaprolactone (PCL) fibres by phase separation, Eur. Polym. J. 69 (2015) 284–295, https://doi.org/10.1016/j.eurpolymj.2015.01.028.

[49] M. Barrejón, S. Marchesan, N. Alegret, M. Prato, Carbon nanotubes for cardiac tissue regeneration: state of the art and perspectives, Carbon 184 (2021) 641–650, https://doi.org/10.1016/j.carbon.2021.08.059.

[50] A. Chalard, et al., Simple synthetic molecular hydrogels from self-assembling alkylgalactonamides as scaffold for 3D neuronal cell growth, ACS Appl. Mater. Interfaces 10 (20) (2018) 17004–17017, https://doi.org/10.1021/acsami.8b01365.

[51] N. Kasmi, et al., The potential of carbohydrate supramolecular hydrogels for long-term 3D culture of primary fibroblasts, J. Mater. Chem. B 13 (14) (2025) 4386–4405, https://doi.org/10.1039/D4TB02658F.

[52] F. Andriamiseza, S. Peters, C. Roux, N. Dietrich, C. Coudret, J. Fitremann, Wet spinning and 3D printing of supramolecular hydrogels in acid-base and dynamic conditions, Colloids Surf. A Physicochem. Eng. Asp. 673 (2023) 131765, https://doi.org/10.1016/j.colsurfa.2023.131765.

[53] J. Gao, et al., Slow kinetic evolution of nanohelices based on gemini surfactant self-assemblies with various enantiomeric excess; chiral segregation towards a racemic mixture, Mater. Chem. Front. 5 (7) (2021) 3021–3028, https://doi.org/10.1039/D0QM00989J.

[54] T.G. Barclay, K. Constantopoulos, J. Matisons, Nanotubes self-assembled from amphiphilic molecules via helical intermediates, Chem. Rev. 114 (20) (2014) 10217–10291, https://doi.org/10.1021/cr400085m.

[55] F. Andriamiseza, D. Bordignon, B. Payré, L. Vaysse, J. Fitremann, 3D printing of biocompatible low molecular weight gels: imbricated structures with sacrificial and persistent N-alkyl-d-galactonamides, J. Colloid Interface Sci. 617 (2022) 156–170, https://doi.org/10.1016/j.jcis.2022.02.076.

[56] J.M. Zatorski, A.N. Montalbine, J.E. Ortiz-Cárdenas, R.R. Pompano, Quantification of fractional and absolute functionalization of gelatin hydrogels by optimized ninhydrin assay and 1H NMR, Anal. Bioanal. Chem. 412 (24) (2020) 6211–6220, https://doi.org/10.1007/s00216-020-02792-5.

[57] H. R. Hertz, "Uber die Beruhrung fester elastischer Korper und uber die Harte," *Verhandlung des Vereins zur Beforderung des GewerbefleiBes, Berlin*, vol. 0, p. 449, 1882.

[58] G.N. Greaves, A.L. Greer, R.S. Lakes, T. Rouxel, Poisson's ratio and modern materials, Nat. Mater. 10 (11) (2011) 823–837, https://doi.org/10.1038/nmat3134.

[59] E.P. Gilbert, J.C. Schulz, T.J. Noakes, 'Quokka'—the small-angle neutron scattering instrument at OPAL, Phys. B Condens. Matter 385–386 (2006) 1180–1182, https://doi.org/10.1016/j.physb.2006.05.385.

[60] S.R. Kline, Reduction and analysis of SANS and USANS data using IGOR pro, J. Appl. Cryst. 39 (6) (2006) 895–900, https://doi.org/10.1107/S0021889806035059.

[61] P.V. Konarev, V.V. Volkov, A.V. Sokolova, M.H.J. Koch, D.I. Svergun, *PRIMUS*: a windows PC-based system for small-angle scattering data analysis, J. Appl. Cryst. 36 (5) (2003) 1277–1282, https://doi.org/10.1107/S0021889803012779.

[62] C. Rehm, A. Brûlé, A.K. Freund, S.J. Kennedy, Kookaburra: the ultra-small-angle neutron scattering instrument at OPAL, J. Appl. Cryst. 46 (6) (2013) 1699–1704, https://doi.org/10.1107/S0021889813025788.

[63] J.C. Villalobos Lizardi, et al., A guide for assessment of myocardial stiffness in health and disease, Nat. Cardiovasc. Res. 1 (1) (2022) 8–22, https://doi.org/10.1038/s44161-021-00007-3.
[64] A. Miyazawa, et al., Regulation of PD-L1 expression by matrix stiffness in lung cancer cells, Biochem. Biophys. Res. Commun. 495 (3) (2018) 2344–2349, https://doi.org/10.1016/j.bbrc.2017.12.115.
[65] J.J.H.M. Smits, A. Van Der Pol, M.J. Goumans, C.V.C. Bouten, I. Jorba, GelMA hydrogel dual photo-crosslinking to dynamically modulate ECM stiffness, Front. Bioeng. Biotechnol. 12 (2024) 1363525, https://doi.org/10.3389/fbioe.2024.1363525.
[66] K. Amitani, K. Terao, Y. Nakamura, T. Norisuye, Small-angle X-ray scattering from polystyrene polymacromonomers in cyclohexane, Polym. J. 37 (4) (2005) 324–331, https://doi.org/10.1295/polymj.37.324.
[67] V. Receveur-Brechot, D. Durand, How random are intrinsically disordered proteins? A small angle scattering perspective, CPPS 13 (1) (2012) 55–75, https://doi.org/10.2174/138920312799277901.
[68] V.M. Burger, D.J. Arenas, C.M. Stultz, A structure-free method for quantifying conformational flexibility in proteins, Sci. Rep. 6 (1) (2016) 29040, https://doi.org/10.1038/srep29040.
[69] P. Beckrich, A. Johner, A.N. Semenov, S.P. Obukhov, H. Benoît, J.P. Wittmer, Intramolecular form factor in dense polymer systems: systematic deviations from the Debye formula, Macromolecules 40 (10) (2007) 3805–3814, https://doi.org/10.1021/ma0626113.
[70] B. Hammouda, D.L. Ho, S. Kline, Insight into clustering in poly(ethylene oxide) solutions, Macromolecules 37 (18) (2004) 6932–6937, https://doi.org/10.1021/ma049623d.
[71] M.-R. Dobrisan, A. Lungu, M. Ionita, A review of the current state of the art in gelatin methacryloyl-based printing inks in bone tissue engineering, Virtual Phys. Prototyp. 19 (1) (2024) e2378003, https://doi.org/10.1080/17452759.2024.2378003.
[72] Y. Chen, et al., Functional human vascular network generated in photocrosslinkable gelatin methacrylate hydrogels, Adv. Funct. Mater. 22 (10) (2012) 2027–2039, https://doi.org/10.1002/adfm.201101662.
[73] I. Noshadi, et al., In vitro and in vivo analysis of visible light crosslinkable gelatin methacryloyl (GelMA) hydrogels, Biomater. Sci. 5 (10) (2017) 2093–2105, https://doi.org/10.1039/C7BM00110J.
[74] S. Krishnamoorthy, B. Noorani, C. Xu, Effects of encapsulated cells on the physical–mechanical properties and microstructure of gelatin methacrylate hydrogels, IJMS 20 (20) (2019) 5061, https://doi.org/10.3390/ijms20205061.
[75] A. Forgács, et al., Mechanism of hydration and hydration induced structural changes of calcium alginate aerogel, ACS Appl. Mater. Interfaces 13 (2) (2021) 2997–3010, https://doi.org/10.1021/acsami.0c17012.
[76] P. Lopez-Sanchez, A. Assifaoui, F. Cousin, J. Moser, M.R. Bonilla, A. Ström, Impact of glucose on the nanostructure and mechanical properties of calcium-alginate hydrogels, Gels 8 (2) (2022) 71, https://doi.org/10.3390/gels8020071.
[77] P.N. Depta, et al., DEM-based approach for the modeling of gelation and its application to alginate, J. Chem. Inf. Model. 62 (1) (2022) 49–70, https://doi.org/10.1021/acs.jcim.1c01076.
[78] A. Borzacchiello, L. Russo, B.M. Malle, K. Schwach-Abdellaoui, L. Ambrosio, Hyaluronic acid based hydrogels for regenerative medicine applications, Biomed. Res. Int. 2015 (2015) 871218, https://doi.org/10.1155/2015/871218.
[79] E.M. Saffer, M.A. Lackey, D.M. Griffin, S. Kishore, G.N. Tew, S.R. Bhatia, SANS study of highly resilient poly(ethylene glycol) hydrogels, Soft Matter 10 (12) (2014) 1905, https://doi.org/10.1039/c3sm52395k.
[80] R. Chen, Z. Li, J. He, Determination of upper limit of Guinier approximation on dilute polydisperse system in SAXS, Nucl. Instrum. Methods Phys. Res., Sect. B 552 (2024) 165377, https://doi.org/10.1016/j.nimb.2024.165377.
[81] D. McDowall, D.J. Adams, A.M. Seddon, Using small angle scattering to understand low molecular weight gels, Soft Matter 18 (8) (2022) 1577–1590, https://doi.org/10.1039/D1SM01707A.
[82] B. Hammouda, A new Guinier–Porod model, J. Appl. Cryst. 43 (4) (2010) 716–719, https://doi.org/10.1107/S0021889810015773.
[83] M. Shibayama, Small-angle neutron scattering on polymer gels: phase behavior, inhomogeneities and deformation mechanisms, Polym. J. 43 (1) (2011) 18–34, https://doi.org/10.1038/pj.2010.110.
[84] Y. Gombert, F. Roncoroni, A. Sánchez-Ferrer, N.D. Spencer, The hierarchical bulk molecular structure of poly(acrylamide) hydrogels: beyond the fishing net, Soft Matter 16 (42) (2020) 9789–9798, https://doi.org/10.1039/D0SM01536A.
[85] C. Neylon, Small angle neutron and X-ray scattering in structural biology: recent examples from the literature, Eur. Biophys. J. 37 (5) (2008) 531–541, https://doi.org/10.1007/s00249-008-0259-2.